

APPENDICES FOR CHAPTER 9

9-A NONLINEAR LAGRANGIAN TWT MODEL

For this model, one breaks the continuous beam into a finite number of N "disks," each labeled by their respective initial phase $\psi_{0j} = -\omega_0 t_{0j}$ with $j = 1, \dots, N$. The time over which disks are spread is one fundamental period $2\pi / \omega_0$ (see Fig. 9.5) so we have

$$\psi_{0j} = -2\pi \frac{j-1}{N} \quad j = 1, \dots, N \quad (\text{A.1})$$

The velocity and phase position of each disk are notated as $v_j = v(z, \psi_{0j})$ and $\Psi_j = \Psi(z, \psi_{0j})$ respectively.

To obtain the large signal model, one computes the Fourier coefficients of the first three equations of Eqs. (9.8) based on the Fourier synthesis equation (9.10), where the Fourier coefficient integral of the charge density in Eulerian coordinates

$$\tilde{\rho}_\ell = \frac{1}{2\pi} \int_0^{2\pi} \rho(z, \psi) e^{-j\ell\psi} d\psi \quad (\text{A.2})$$

is converted to Lagrangian coordinates [1]

$$\tilde{\rho}_\ell = \frac{1}{2\pi} \int_0^{2\pi} \frac{I_0(\psi_0) e^{-j\ell\Psi(z, \psi_0)}}{Av(z, \psi_0)} d\psi_0 \quad (\text{A.3})$$

where $I_0(\psi_0)$ is the initial beam current. Equations (9.8) are converted to Lagrangian coordinates by using the Fourier synthesis form (9.10) for the field variables $V(z, \psi)$ and $E(z, \psi)$, and including a differential equation for Ψ_j . This yields the TWT Lagrangian model:

$$\begin{aligned}
\frac{d\tilde{V}_\ell}{dz} &= -\frac{if_\ell\omega_0}{u_0}\tilde{V}_\ell - \frac{if_\ell\omega_0}{\tilde{v}_{ph}(f_\ell\omega_0)}\tilde{K}(f_\ell\omega_0)\tilde{I}_\ell \\
\frac{d\tilde{I}_\ell}{dz} &= -\frac{if_\ell\omega_0}{\tilde{K}(f_\ell\omega_0)\tilde{v}_{ph}(f_\ell\omega_0)}\tilde{V}_\ell - \frac{if_\ell\omega_0}{u_0}\tilde{I}_\ell + if_\ell\omega_0\frac{1}{N}\sum_{j=1}^N\frac{I_0(\psi_{0j})e^{-if_\ell\Psi_j}}{v_j} \\
\frac{d\tilde{E}_\ell}{dz} &= -\frac{if_\ell\omega_0}{u_0}\tilde{E}_\ell + \frac{1}{\varepsilon_0 A}\frac{1}{N}\sum_{j=1}^N\frac{I_0(\psi_{0j})e^{-if_\ell\Psi_j}}{v_j} \\
\frac{dv_j}{dz} &= \frac{1}{v_j}\sum_{\ell=-M}^M\left\{\frac{if_\ell\omega_0 e\tilde{K}(f_\ell\omega_0)}{m_e\tilde{v}_{ph}(f_\ell\omega_0)}\tilde{I}_\ell + \frac{e}{m_e}\tilde{R}(f_\ell\omega_0)\tilde{E}_\ell\right\}e^{if_\ell\Psi_j} \\
\frac{d\Psi_j}{dz} &= \frac{\omega_0}{u_0}\left(1 - \frac{u_0}{v_j}\right)
\end{aligned} \tag{A.4}$$

where $\ell = -M, \dots, M$ and $j = 1, \dots, N$. In Eqs. (A.4) the integrals in the charge density Fourier coefficient formula have been replaced by sums over the finite number of disks. Furthermore we have truncated the sum over frequencies to a finite number $\ell = -M, \dots, M$. These equations represent $6M$ total equations since each frequency $f_\ell\omega_0$ has a negative frequency counterpart $-f_\ell\omega_0$, owing to our Fourier series representation of the real valued functions V , I , and E .

There are N equations for v_j and Ψ_j , one for each of the N disks.

The circuit power at angular frequency ω is due to both the positive and negative frequencies, so

$$P_\omega(z) = -[\tilde{V}_\ell(z)\tilde{I}_\ell^*(z) + \tilde{V}_\ell^*(z)\tilde{I}_\ell(z)] \tag{A.5}$$

where the negative sign in Eq. (A.5) is due to the form of the telegrapher equations that were chosen. Given input power $P_\omega(0)$ and phase $\varphi_\omega(0)$ at $\omega = f_\ell \omega_0 > 0$, the initial value of circuit voltage is

$$\tilde{V}_\ell(0) = \sqrt{\frac{P_\omega(0) \tilde{K}(f_\ell \omega_0)}{2}} e^{i\varphi_\omega(0)} \quad (\text{A.6})$$

where $\tilde{V}_{-\ell}(0) = \tilde{V}_\ell^*(0)$, and

$$\tilde{I}_\ell(0) = -\frac{\tilde{V}_\ell(0)}{\tilde{K}(f_\ell \omega_0)} \quad (\text{A.7})$$

Model equations (A.4) are known as LATTE (Lagrangian TWT Equations)

9-B S-MUSE NONLINEAR EULERIAN TWT MODEL

Another useful nonlinear TWT model can be derived from Eqs. (9.8) by using a Fourier series representation for the electron beam velocity v and density ρ . Computing the Fourier coefficients of Eqs. (9.8) based on the Fourier synthesis equation (9.10), and neglecting certain nonlinearities [1] one gets

$$\begin{aligned}
\frac{d \tilde{V}_\ell}{dz} &= -\frac{if_\ell \omega_0}{u_0} \tilde{V}_\ell - \frac{if_\ell \omega_0 \tilde{K}(f_\ell \omega_0)}{\tilde{v}_{ph}(f_\ell \omega_0)} \tilde{I}_\ell \\
\frac{d \tilde{I}_\ell}{dz} &= -\frac{if_\ell \omega_0}{\tilde{K}(f_\ell \omega_0) \tilde{v}_{ph}(f_\ell \omega_0)} \tilde{V}_\ell - \frac{if_\ell \omega_0}{u_0} \tilde{I}_\ell + if_\ell \omega_0 A \tilde{\rho}_\ell \\
\frac{d \tilde{E}_\ell}{dz} &= -\frac{if_\ell \omega_0}{u_0} \tilde{E}_\ell + \frac{\tilde{\rho}_\ell}{\varepsilon_0} \\
\frac{d \tilde{v}_\ell}{dz} &= \frac{if_\ell \omega_0 e \tilde{K}(f_\ell \omega_0)}{m_e u_0 \tilde{v}_{ph}(f_\ell \omega_0)} \tilde{I}_\ell + \frac{e}{m_e u_0} \tilde{R}(f_\ell \omega_0) \tilde{E}_\ell - \frac{1}{u_0^2} \sum_{m \neq 0, n \neq 0, f_m + f_n = f_\ell} if_n \omega_0 \tilde{v}_m \tilde{v}_n \\
\frac{d \tilde{\rho}_\ell}{dz} &= -\frac{if_\ell \omega_0 e \rho_0 \tilde{K}(f_\ell \omega_0)}{m_e u_0^2 \tilde{v}_{ph}(f_\ell \omega_0)} \tilde{I}_\ell - \frac{e \rho_0}{m_e u_0^2} \tilde{R}(f_\ell \omega_0) \tilde{E}_\ell - \frac{if_\ell \omega_0 \rho_0}{u_0^2} \tilde{v}_\ell \\
&\quad - \frac{e}{m_e u_0^2} \sum_{m \neq 0, n \neq 0, f_m + f_n = f_\ell} \frac{if_m \omega_0 \tilde{K}(f_m \omega_0)}{\tilde{v}_{ph}(f_m \omega_0)} \tilde{I}_m \tilde{\rho}_n - \frac{e}{m_e u_0^2} \sum_{m \neq 0, n \neq 0, f_m + f_n = f_\ell} \tilde{R}(f_m \omega_0) \tilde{E}_m \tilde{\rho}_n \\
&\quad + \frac{\rho_0}{u_0^3} \sum_{m \neq 0, n \neq 0, f_m + f_n = f_\ell} if_n \omega_0 \tilde{v}_m \tilde{v}_n - \frac{if_\ell \omega_0}{u_0^2} \sum_{m \neq 0, n \neq 0, f_m + f_n = f_\ell} \tilde{v}_m \tilde{\rho}_n
\end{aligned} \tag{A.8}$$

where ρ_0 is the dc beam charge density and $-M \leq \ell \leq M, \ell \neq 0$. The input and output power relationships with circuit voltage and current are given by Eqs. (A.5 – A.7).

Equations (A.8) are known as the S-MUSE model, and are a simplification of the MUSE model. The MUSE model is the result of spectral analysis of Eqs. (9.8) where no nonlinearities are neglected. Here we will be mostly interested in the analytic solution to the S-MUSE model, which can be considered as an approximate analytic solution to the LATTE equations that applies at power levels below saturation. For a detailed comparison of the LATTE and S-MUSE models the reader is referred to [1].

To find the analytic solution to the S-MUSE equations we use the vector notation found in [1], where $x_\ell = [x_{\ell_1} \dots x_{\ell_s}]^T = [\tilde{V}_\ell \tilde{I}_\ell \tilde{E}_\ell \tilde{v}_\ell \tilde{\rho}_\ell]^T$. Due to the Fourier series used in the model, for each positive frequency $f_\ell \omega_0$ there is a corresponding negative frequency indexed by $-\ell$ with $f_{-\ell} = -f_\ell$. Furthermore $x_{-\ell} = x_\ell^*$. Equations (A.8) are written as the vector differential equation for x_ℓ

$$\frac{dx_\ell}{dz} = A_\ell x_\ell + \sum_{f_m + f_n = f_\ell} H_{\ell mn}(x_m, x_n) \quad (\text{A.9})$$

where matrix and tensor components $A_{\ell_{ij}}$ and $H_{\ell_{ijm_j n_k}}$ are given in [1]. In Eq. (A.9) the product $A_\ell x_\ell$ contains the linear terms of Eqs. (A.8), and $\sum H_{\ell mn}(x_m, x_n)$ represents the quadratic terms.

One can show that Eq. (A.9) may be solved with a series solution

$$x_\ell = \sum_{\alpha=1}^{\infty} x_\ell^{(\alpha)} \quad (\text{A.10})$$

and that this series converges under the appropriate conditions [2]. The formulas for the terms of the series are given by

$$x_\ell^{(1)} = e^{A_\ell z} w_\ell \quad \alpha = 1 \quad (\text{A.11})$$

$$x_\ell^{(\alpha)} = \int_0^z e^{A_\ell(z-\tau)} \sum_{\beta=1}^{\alpha-1} \sum_{f_m+f_n=f_\ell} H_{\ell mn}(x_m^{(\beta)}(\tau), x_n^{(\alpha-\beta)}(\tau)) d\tau \quad \alpha \geq 2 \quad (\text{A.12})$$

where w_ℓ contains the initial values of frequency $f_\ell \omega_0$ and $e^{A_\ell z}$ is the matrix exponential of the matrix $A_\ell z$ [3]. The complex exponential modes of the vector $x_\ell^{(\alpha)}$ may be indexed by p

$$x_\ell^{(\alpha)}(z) = \sum_{p=1}^{N_\ell^{(\alpha)}} a_\ell^{(\alpha)[p]} e^{(\mu_\ell^{(\alpha)[p]} + i\sigma_\ell^{(\alpha)[p]})z} \quad (\text{A.13})$$

with $a_\ell^{(\alpha)[p]}$ a complex vector, and $\mu_\ell^{(\alpha)[p]}, \sigma_\ell^{(\alpha)[p]}$ real numbers. Sums like Eq. (A.13) are ordered

so that $\mu_\ell^{(\alpha)[1]} \geq \mu_\ell^{(\alpha)[2]} \geq \dots \geq \mu_\ell^{(\alpha)[N_\ell^{(\alpha)}]}$. General formulas to compute the terms of Eq. (A.13) are given in [2].

9-D CONSIDERATIONS FOR COMMUNICATIONS TWTs

It is important to minimize the length of a communication TWT in order to reduce the material and magnet costs. The parameters that determine the length are given by simple small signal TWT theory. Following Pierce [4], the gain is given by

$$\text{Gain} = A + BCN, \quad (\text{A.14})$$

where A and B are constants, C is the Pierce gain parameter, and N is the number of wavelengths in the system. The Pierce gain parameter is

$$C^3 = \frac{Z_c}{4Z_b}, \quad (\text{A.15})$$

where Z_c is the helix circuit impedance and Z_b is the electron beam impedance. The electron beam impedance is given by

$$Z_b = \frac{V}{I} = \frac{1}{PV^{1/2}}, \quad (\text{A.16})$$

where V is the beam voltage, I is the beam current, and P is the beam perveance defined as $I/V^{3/2}$. The number of wavelengths on the helix for a resonant wave is approximately

$$N \approx \frac{f}{u_o} L, \quad (\text{A.17})$$

where f is the operating frequency, u_o is the beam velocity and L is the length of the helix.

Substituting Eqs. (A.15-A.17) into Eq. (A.14) gives

$$\text{Gain} = A + \frac{fBL}{u_o} \left[\frac{Z_c PV^{1/2}}{4} \right]^{\frac{1}{3}}. \quad (\text{A.18})$$

By taking the beam voltage dependence out of the beam velocity, grouping all the constants in a term k, and neglecting the constant A, which is related to input drive losses, we find the length of the helix is

$$L = \frac{\text{Gain}}{k f} \left(\frac{V}{P Z_c} \right)^{\frac{1}{3}} \quad (\text{A.19})$$

The length of the helix, and therefore the length of the tube, is minimized by choosing the smallest required gain, the maximum perveance and the highest helix impedance. A more sophisticated analysis of the helix length that includes effects like loss, space charge, and non-linear large signals yields a similar dependence of the helix length in Eq. (A.19) on perveance and gain [5].

In TWTs, the harmonics and intermods usually have a decreasing amplitude with increasing order. This is illustrated in Figure A-1, where the power level of eight equal amplitude signals of different frequencies and with randomly varying phase from a TWT amplifier are shown as a function of frequency. We see that the generated third-order IMD signals are about 30 dB below the carrier signals, and the fifth-order IMD signals are over 50 dB down.

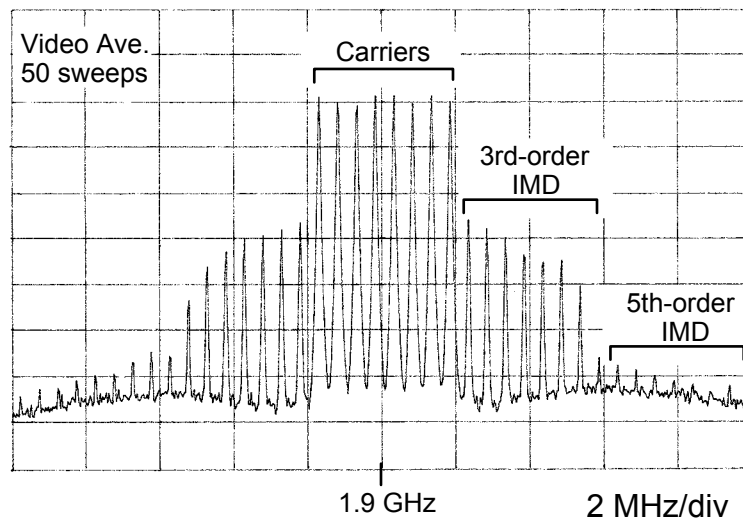


Figure A-1 Spectrum analyzer signal (power versus frequency) for a 8 signal cell phone simulator at 150 W of average power from a Boeing 422H TWT amplifier with continuously varying signal phases.

Typical AM/AM and AM/PM transfer curves for a Boeing 5525H communications TWT are shown in Figure A-2. The AM/AM curve shows the characteristic linear performance of the amplifier at small signal, and then saturation of the output power for this TWT at just over 63.2 dBm (2.1 kW). The AM/PM curve shows the change in phase relative to the input power. These tubes typically have a phase change of slightly less than 40° at saturation relative to zero phase at small signal. The maximum phase change with drive level from the derivative of the AM/PM curve for this TWT is 2.2 degrees/dB. In all cases, the transfer curves are smooth and continuous, which is characteristic of this TWT circuit design that was optimized for high efficiency and low intermodulation products.

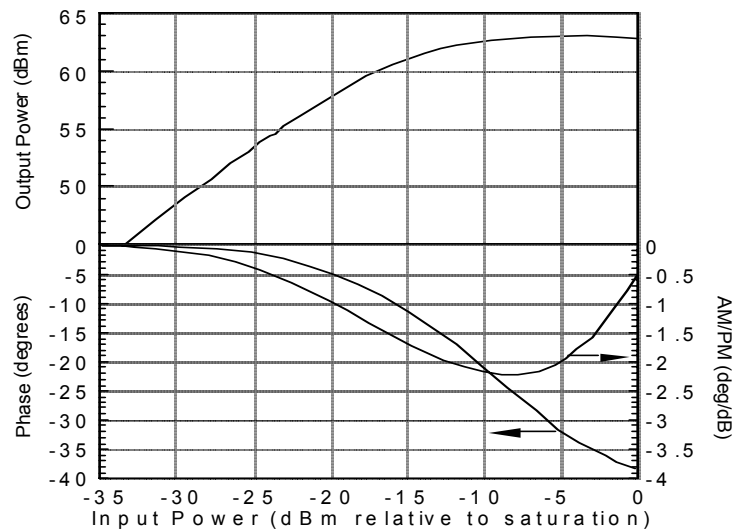


Figure A-2 Typical output power, and phase and the derivative of the phase transfer curves versus input drive level for a 5525H TWT. The maximum AM/PM was found to be about 2.2 deg/dB for this TWT.

Figure A-3 shows the gain of a 5525H TWT as a function of input drive level. The gain is calculated by dividing the output power by the input power, and typically ranges from 40 to 44

dB with an average value of 42 dB small signal gain for these devices. In the figure, the gain remains relatively unchanged as the drive level is increased from small signal, and then starts to decrease at input drive levels 15 to 20 dB below saturation. The 1-dB gain compression point (where the gain has decreased by 1 dB relative to small signal) occurs at about 12.5 dB below the drive level required to obtain saturation for this MVED. The gain compression at saturation is about 9.5 dB, which is larger than most space TWTs designed for maximum efficiency at saturation, and results from the circuit design in this TWT that was optimized for linearity and the ability to match a passive predistorter. The characteristics of the transfer curves determine the linearity of the amplifier, which ultimately determine the IMD performance of the amplifier.

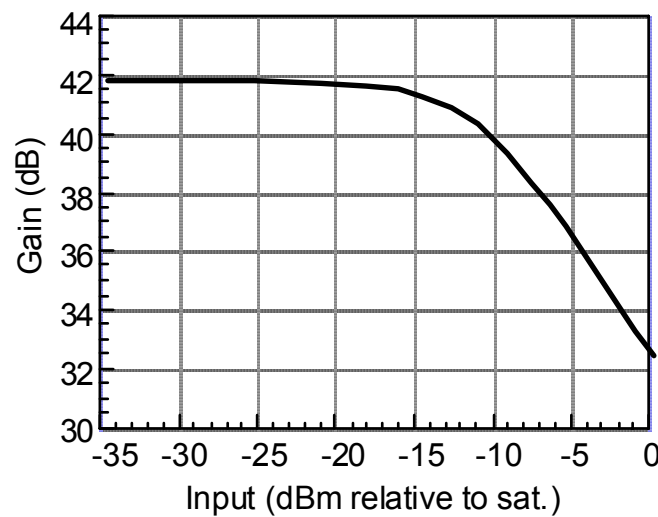


Figure A-3 Typical gain compression curve for a communications TWT.

9-C AN OVERVIEW OF TWT POWER-COMBINING

For situations where the peak and/or average power level required by the communications system designer to close the link exceeds that available from a single TWT, it is possible to efficiently power combine the TWT outputs. However, the challenge is to combine the output of TWTs optimized for high linearity and carrying many signals of varying phase simultaneously. Avoiding power combining losses requires that the average phase response of the TWTs is consistent, and does not change over time or as a result of environmental conditions.

To establish the effectiveness of power combining communications TWTs, the phase versus drive of 35 Boeing 5525H TWTs was measured [6]. As shown previously, this S-band TWT normally operates 6 to 10 dB backed off from about 2.1 kW of power at saturation, and can produce over 525 W of average output power at an efficiency of nearly 40%. For these experiments, each TWT was swept from small signal to saturation by a HP/Agilent vector network analyzer. Measurements of the phase, gain and AM/PM conversion were made for each of the TWTs, and the power loss associated with combining all 35 TWTs with the measured performance variation was determined.

Figure A-4 shows the phase change versus drive for all 35 TWTs tested. In these data, the output phase of all the TWTs at small signal (35 dB below saturation) was normalized to zero. Figure A-4 shows on average the TWTs have a phase change at saturation of 35° with a total variation of about $\pm 5^\circ$. However, if the reference point for zero phase was chosen for all of the TWTs to be matched at the normal operating point of 6 dB average output back off (525W), the average change in phase was only 26° with a total variation in phase for the 35 TWTs of only 7.68° ($\pm 3.8^\circ$). For power combining applications where the phase is matched up at the nominal operating point (525 W average in this case), the change in phase produced by multiple tones

causing momentary transitions to saturation and beyond is smaller than the characteristic total phase change from small signal to saturation. A histogram plot is useful to show the distribution in phase change measured at saturation. Figure A-5 shows this representation with the plot of phase change at saturation compared to the mean versus the number of TWTs that were found at each level. The plot shows that the TWTs have a distribution about the mean with a standard deviation of only 2.6 degrees.

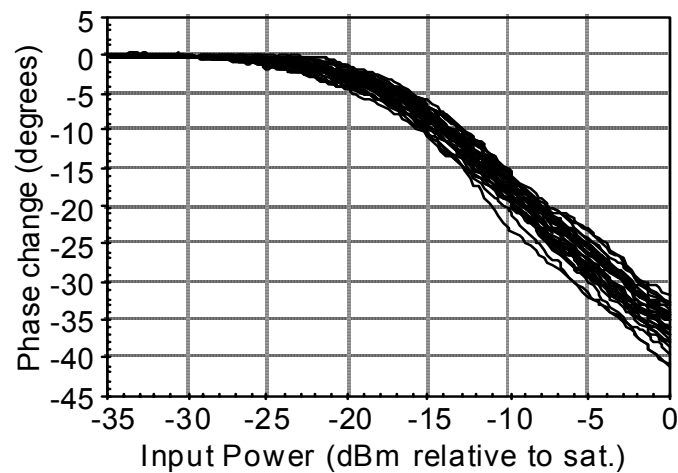


Figure A-4 Phase change relative to small signal versus input drive level for 35 S-band 5525H TWTs.

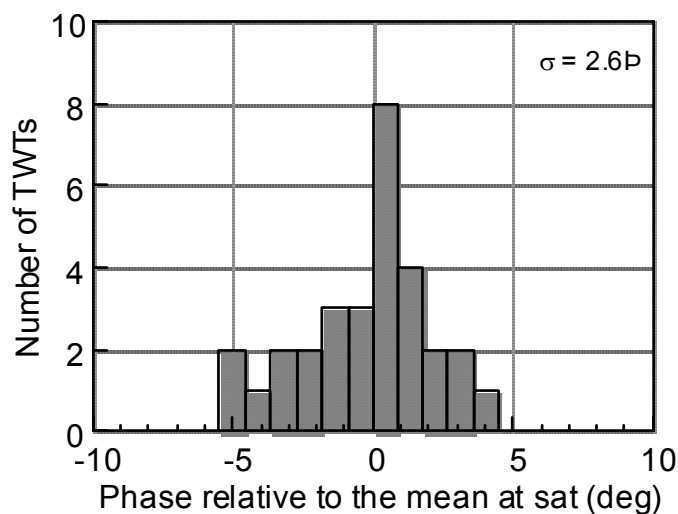


Figure A-5 Phase histogram for the 35 TWTs tested showing a standard deviation in phase at saturation of only 2.6°.

The derivative of the phase versus drive curve provides the AM/PM conversion in degrees per dB [6].

Figure A-6 shows a plot of the AM/PM transfer curve obtained from 24 of the TWTs tested. The maximum AM/PM conversion is seen to occur at about 10 dB input back off from saturation, and has a mean value of 2.09 degrees per dB. Figure A-7 shows a histogram of the maximum AM/PM conversion for each of these TWTs. The maximum AM/PM conversion values are distributed uniformly about the mean value with a standard deviation of 0.16 deg/dB.

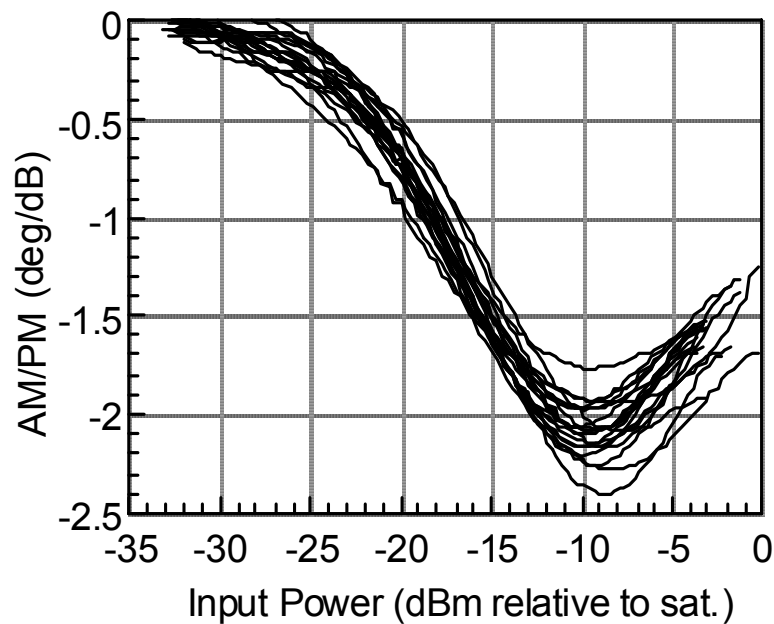


Figure A-6 AM/PM transfer curves showing the conversion value versus input drive

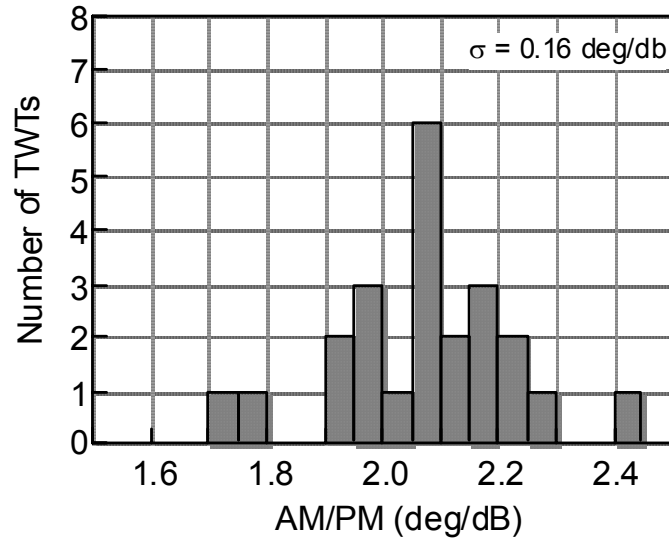


Figure A-7 Histogram of the AM/PM conversion showing a mean value for the TWTs of 2.09 deg/dB and a standard deviation of 0.16.

Figure A-8 shows the gain compression curves measured for all 35 of the TWTs. In this case, the gains of all the TWTs were normalized at 15 dB input drive below saturation corresponding to the rated average power point. The average gain compression at saturation is 9.5 dB with a total variation of about 1 dB. Figure A-9 shows a histogram of the gain data, which shows the gain has a Gaussian distribution about the mean at saturation with a standard deviation of 0.22 dB. It is likely that the variation in gain at saturation is due to either some manufacturing tolerance in building the TWT, or the uncertainty in finding the exact saturated point and determining the gain at that point. The losses that are associated with gain and phase variation in power combined TWTs are not the only losses one would expect in a power combining system. Other losses will occur in external components such as waveguides, combiners, and power splitters. Variations in the TWT transfer curves with temperature and lifetime will also play a role.

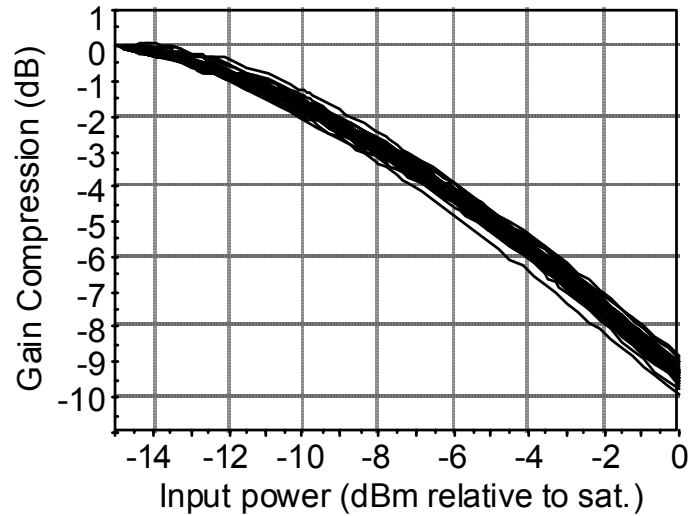


Figure A-8 Gain versus input drive relative to saturation for all 35 S-Band TWTs showing an average of 9.5 dB gain compression at saturation for these TWTs.

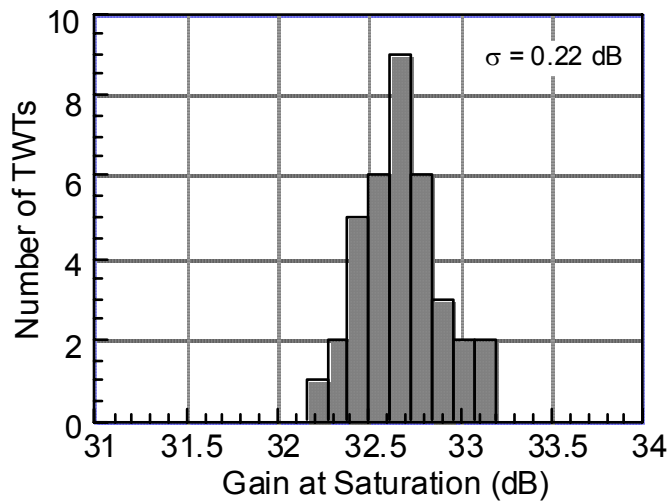


Figure A-9 Gain histogram for the 35 S-Band TWTs at saturation. The TWTs had a standard deviation in gain at saturation of only 0.22 dB.

These loss characteristics are also observed in other space TWTs designed to operate continuously at saturation at frequencies up to Ku-Band. Table A.1 shows the phase and gain compressions at saturation for the S-band TWTs and for a variety of space TWTs. The S-Band 5525H TWT has a higher phase shift variation at saturation compared to the other TWTs. This is

primarily because the phase of a space TWT is adjusted and optimized at saturation per specification, whereas the S-Band TWT is optimized for high linearity and efficiency when backed off 6 to 8 dB from saturation. The S-Band TWT design also resulted in higher gain compression at saturation than the other TWTs. Nevertheless, the standard deviation of the gain at saturation is consistent between all the TWTs. This similarity occurs because phase shift variation and gain variation are due to variations in the non-linear TWT interaction that are sensitive to differences in operating voltage, circuit phase velocity and the TWT basic efficiency. All of these factors are sensitive to manufacturing tolerance and variability in parts of the TWT such as helix pitch, rod sizes, rod composition and dielectric uniformity, gun alignment and magnetic focusing.

Table A.1 Typical phase and gain performance at saturation for various TWTs.

| Frequency Band | Number of TWTs | Ave. phase shift at sat. (degrees) | Phase σ at saturation (degrees) | Gain compression at sat (dB) | Gain σ at saturation (dB) |
|----------------|----------------|------------------------------------|--|------------------------------|----------------------------------|
| Ku (120 W) | 40 | 42.6 | 1.8 | 7.6 | 0.4 |
| Ku (30 W) | 14 | 42.5 | 1.6 | 5.9 | 0.24 |
| X (100 W) | 27 | 39.3 | 1.5 | 6.9 | 0.21 |
| C (60 W) | 24 | 37.4 | 1.1 | 7.4 | 0.3 |
| S (525W ave.) | 35 | 35 | 2.6 | 9.5 | 0.22 |

Efficient combining of the power from TWTs requires good matching of the phase and gain characteristics. When combining two signals of the same frequency but with a phase difference of $\Delta\phi$ [7], the total power out is

$$P = \frac{1}{2} \left[P_1 + P_2 + 2(P_1 P_2)^{1/2} \cos\Delta\phi \right], \quad (\text{A.20})$$

where P1 is the power of the first signal and P2 is the power of the second signal. The reduction in the output power from this expression, expressed as combining loss, is shown in Figure A-10 as a function of power and phase imbalance. Differences in gain of over 0.5 dB and phase of over several degrees are required to get an appreciable combining loss and reduction in output power.

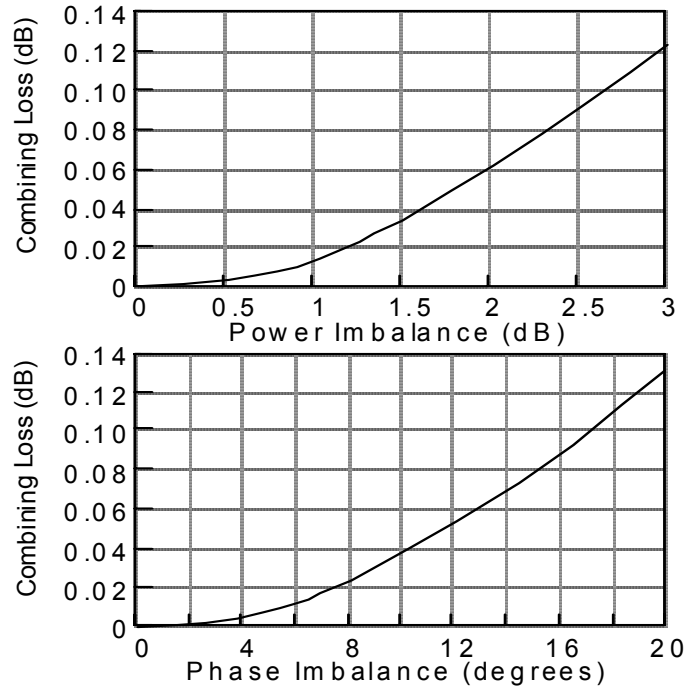


Figure A-10 Power combining losses as a function of power level and phase difference for signals from two amplifiers.

If the signal is fed into the two amplifiers from a common pre-amplifier with a signal power of P_s , then the difference in power of the two signals can be related to the difference in gain of the two TWTs. Equation (A.20) then becomes

$$P = \frac{P_s}{2} \left[G_1 + G_2 + 2(G_1 G_2)^{1/2} \cos \Delta \phi \right] \quad (A.21)$$

For a difference in gain between the two amplifiers $\Delta G = G_1 - G_2$, the combined output power is

$$P = \frac{P_s}{2} \left[2G_1 - \Delta G + 2(G_1^2 - G_1 \Delta G)^{1/2} \cos \Delta \phi \right]. \quad (\text{A.22})$$

This expression applies at all drive levels along the transfer curve, but the power is affected most at saturation where the phase and gain differences are the largest. For the case of selecting two TWTs with the maximum 10° phase difference and 1 dB gain difference, the output power is reduced by 1.09%. For the nominal case described by two TWTs with the standard deviations in phase and gain of $\pm\sigma$, the total phase difference is 3.2° and the gain difference is 0.44 dB, resulting in a power output reduced by 0.68%. If we phase-combine a large number of TWTs all at the same time, Eq. (A.20) applies if the average phase difference $2\Phi/\sqrt{\pi}$ is used, where Φ is the standard phase deviation. For the 35 TWTs discussed here, a loss of less than 1% of the power at saturation is found due to the phase and gain deviations.

In most applications, multiple amplifiers are combined in even groups such that $2n$ TWTs are combined in n -levels. If the TWTs have an average rf output power P and a Gaussian distribution in total phase with a standard phase deviation of Φ , then the total combined power (neglecting ohmic losses in the combiners) is given by:

$$P_T = 2^n P \prod_{i=1}^n (1 + \cos \phi_i) \quad (\text{A.23})$$

where

$$\phi_i = \frac{2}{\sqrt{\pi}} \frac{\Phi}{(\sqrt{2})^{(i-1)}} \quad (\text{A.24})$$

The $(\sqrt{2})^{(i-1)}$ factor comes because the phases of the power combined TWTs will average out at each combined stage, so the standard deviation will effectively become smaller at each higher

level of combining. Approximating $\cos(x)$ as $\left(1 - \frac{x^2}{2}\right)$ and neglecting the small terms, the total combined power is then

$$P_T = 2^n P \left(1 - \sum_{i=1}^n \frac{\phi_i^2}{4}\right) = 2^n P \left(1 - \sum_{i=1}^n \frac{\Phi^2}{\pi 2^{i-1}}\right) \quad (A.25)$$

For example, for combining eight TWTs, the total power is

$$P_T = 2^3 P \left[1 - \left(1 + \frac{1}{2} + \frac{1}{4}\right) \frac{\Phi^2}{\pi}\right] = 8P \left(1 - \frac{7}{4} \frac{\Phi^2}{\pi}\right) \quad (A.26)$$

If the standard deviation is 5 degrees (0.087266 radians), then the total power output is $0.9958 \cdot 8P$. Again, for relatively small deviations in phase such as measured for the TWTs here, the penalty in power loss in phased combined TWTs is less than 1%. The losses in the other microwave components, such as the waveguides, power combiners, and splitters will normally be larger than this amount in most systems.

In operation backed-off from saturation, these small combining losses will result at all points along the transfer curves. This means that for multi-tone operation where the TWT amplifiers experience varying phase and power associated with the instantaneous addition of the tones [5], the penalty associated with combining multiple power-combined amplifiers is very small. For the case of using predistortion of the signal prior to the amplification by the TWT to improve the linearity and intermodulation performance, it is common to match the predistorter transfer characteristics to each amplifier individually. However, the relatively small variation statistically observed in the TWT transfer curves makes it possible to use a common predistorter driving several amplifiers whose output is power combined with good overall performance.

It is now common practice in communications applications to use multi-beam antennas (MBA) to provide reuse of the available frequency band, improve the contiguous coverage, and

to improve the antenna gain for spot beams [8]. For the case of arrays of feeders for single or multiple apertures (lenses or reflectors), variations in the power and phase of each feed element leads to power efficiency loss and degradation in the edge taper [9]. While the amplitude and phase of the feeder signals is important, variations in feeder phase of several degrees (up to 10° peak-to-peak depending on the configuration) and feeder amplitude of several tenths of dB's has been found to cause negligible degradation in the antenna performance. This level of variation is below those measured in the work reported here. While TWTs are usually used for single feed spot beam applications, power combined communications TWTs such as those described here can be used without significant penalty.

9-E CHAOS AND OPTICAL COMMUNICATIONS PUBLICATIONS

Much of the past research on the use of chaos in communication has been at optical wavelengths. The following is a list of references describing this research:

F.-J. Kao and J.-L. Chern, Coding chaos for information transmission, *Leos Newsletter*, April 1996, pp. 16-19.

L.G. Luo and P.L.Chu, Optical secure communications with chaotic erbium-doped fiber lasers, *J. Opt. Soc. Am. B*, vol. 15, 1998, pp. 2524-2530.

G.D. van Wiggeren and R.Roy, Communication with chaotic lasers, *Science*, vol. 279, 1998, pp. 1198-1200.

S. Tang, H.F. Chen, S.K. Hwang and J.M. Liu, Message encoding and decoding through chaos modulation in chaotic optical communications, *IEEE Trans. Circuits and Systems-I: Fundamental Theory and Appl.*, vol. 49, no.2, Feb. 2002, pp. 163-169.

J. Ohtsubo, Chaos synchronization and chaotic signal masking in semiconductor lasers with optical feedback, *IEEE J. of Quantum Electron.*, vol. 38, no. 9, Sep. 2002, pp. 1141-1154.

S. Tang and J.M. Liu, Synchronization of high-frequency chaotic optical pulses, *Opt. Lett.*, vol.26, 2001, pp. 596-598.

Y. Liu, H.F. Chen, J.M. Liu, P. Davis and T. Aida, Synchronization of optical-feedback-induced chaos in semiconductor lasers by optical injection, *Phys. Rev. A*, vol. 63, 2001, pp. 031 802(R) 1-4.

G.D. VanWiggeren and R. Roy, Communication with chaotic lasers, *Science*, vol. 279, 1998, pp. 1198-1200.

G.D. VanWiggeren and R. Roy, Optical communication with chaotic waveforms, *Phys. Rev. Lett.*, vol. 81, 1998, pp. 3547-3550.

G.D. VanWiggeren and R. Roy, Chaotic communication using time-delayed optical systems, *Int. J. Bifur. Chaos*, vol. 9, 1999, pp. 2129-2156.

H.D.I. Abarbanel, M.B. Kennel, L. Illing, S. Tang, H.F. Chen and J.M. Liu, Synchronization and communication using semiconductor lasers with optoelectronic feedback, *IEEE J. Quantum Electron.*, vol. 37, Oct. 2001, pp. 1301-1311.

A. Sánchez-Díaz, C. Mirasso, P. Colt and P. García-Fernández, Encoded Gbit/s digital communications with synchronized chaotic semiconductor lasers, *IEEE J. Quantum Electron.*, vol. 36, Mar. 1999, pp. 292-297.

S. Sivaprakasam and K.A. Shore, Signal masking for chaotic optical communication using external-cavity diode lasers, *Opt. Lett.*, vol. 24, 1999, pp. 1200-1202.

S. Sivaprakasam and K.A. Shore, Message encoding and decoding using chaotic external-cavity diode lasers, *IEEE J. Quantum Electron.*, vol. 36, Jan. 2000, pp. 35-39.

V. Annovazz-Lodi, S. Donati and A. Scirè, Synchronization of chaotic lasers by optical feedback for cryptographic applications, *IEEE J. Quantum Electron.*, vol. 33, Sept. 1997, pp. 1449-1454.

J.-B. Cuenot, L. Larger, J.-P. Goedgebuer and W.T. Rhodes, Chaos shift keying with an optoelectronic encryption system using chaos in wavelength, *IEEE J. Quantum Electron.*, vol. 37, Jul. 2001, pp. 849-855.

C.R. Mirasso, J. Mulet and C. Masoller, Chaos shift keying encryption in chaotic external-cavity semiconductor lasers using a single-receiver scheme, *IEEE Photon. Tech. Lett.*, vol. 14, 2002, pp. 456-458.

J. Paul, S. Sivaprakasam, P.S. Spencer, P. Rees and K.A. Shore, GHz bandwidth message transmission using chaotic diode lasers, *Electronics Letts*, vol. 38, no. 1, 2002, pp. 28-29.

K.M. Short, Unmasking a modulated chaotic communications scheme, *Int. J. Bifurcation Chaos*, vol. 6, no. 2, 1996, pp. 367-375.

REFERENCES

- [1] Wöhlbier, J.G., J.H. Booske, and I. Dobson, "The Multifrequency Spectral Eulerian (MUSE) model of a traveling wave tube," *IEEE Trans. Plasma Sci.* 30, No. 3 (2002): 1063—1075.
- [2] Wöhlbier, J.G., "Nonlinear Distortion and Suppression in Traveling Wave Tubes: Insights and Methods," Ph.D. thesis, University of Wisconsin--Madison, 2003.
- [3] Coddington, E.A., and N. Levinson, *Theory of Ordinary Differential Equations*, McGraw-Hill, New York, 1955.
- [4] Pierce, J.R., *Traveling Wave Tubes*, Van Nostrand, Princeton, N.J., 1950.
- [5] Goebel, D.M., R.Liou, W. Menninger, "Development of ultra-linear TWT amplifiers for Telecommunications Applications," *IEEE Transactions on Electron Devices* 48 (2001): 74-81.
- [6] Kubasek, S.E., D.M. Goebel, W.L. Menninger, and A.C. Schneider "Power Combining Characteristics of Backed-off Traveling Wave Tubes for Communications Applications," *IEEE Transactions on Electron Devices*, June (2003).
- [7] TWT/TWTA Handbook, 10th Edition published by Boeing Electron Dynamic Devices, Inc., 2002.
- [8] Rao, S.K., "Design and Analysis of Multiple-Beam Reflector Antennas", *IEEE Antennas and Propagation Magazine* 41 (1999): 53-59.
- [9] Iversen, P.O., L.J.Richardi, and W.P.Faust, "A comparison among 1, 3 and 7 horn feeds for a 37-beam MBA," *IEEE Trans. Antennas and Propagation* 42 (1996): 1-8.